RAA 2020 Vol. **20** No. **9**, 147(9pp) doi: 10.1088/1674–4527/20/9/147

http://www.raa-journal.org *http://iopscience.iop.org/raa*

***R**esearch in*
***A**stronomy and*
***A**strophysics*

X-ray absorption and 9.7 μm silicate feature as a probe of AGN torus structure

Jun Xu[1], Mou-Yuan Sun[2], Yong-Quan Xue[1], Jun-Yao Li[1] and Zhi-Cheng He[1]

[1] Department of Astronomy, CAS Key Laboratory for Research in Galaxies and Cosmology, University of Science and Technology of China, Hefei 230026, China; *xuey@ustc.edu.cn*
[2] Department of Astronomy, Xiamen University, Xiamen 361005, China; *msun88@xmu.edu.cn*

Received 2020 March 18; accepted 2020 April 20

Abstract The dusty torus plays a vital role in unifying active galactic nuclei (AGNs). However, the physical structure of the torus remains largely unclear. Here we present a systematical investigation of the torus mid-infrared (MIR) spectroscopic feature, i.e., the 9.7μm silicate line, of 175 AGNs selected from the *Swift*/BAT Spectroscopic Survey (BASS). Our sample is constructed to ensure that each of the 175 AGNs has *Spizter*/IRS MIR, optical, and X-ray spectroscopic coverage. Therefore, we can simultaneously measure the silicate strength, optical emission lines, and X-ray properties (e.g., the column density and the intrinsic X-ray luminosity). We show that, consistent with previous works, the silicate strength is weakly correlated with the hydrogen column density ($N_{\rm H}^{\rm X}$), albeit with large scatters. For X-ray unobscured AGNs, the silicate-strength-derived V-band extinction and the broad-Hα-inferred one are both small; however, for X-ray obscured AGNs, the former is much larger than the latter. In addition, we find that the optical type 1 AGNs with strong X-ray absorption on average show significant silicate absorption, indicating that their X-ray absorption might not be caused by dust-free gas in the broad-line region. Our results suggest that the distribution and structure of the obscuring dusty torus are likely to be very complex. We test our results against the smooth and clumpy torus models and find evidence in favor of the clumpy torus model.

Key words: galaxies: active — infrared: galaxies — quasars: general

1 INTRODUCTION

The dusty torus, which is widely believed to be responsible for obscuring the broad emission-line region and the central engine, is a vital component of the unification models (e.g., Antonucci 1993; Urry & Padovani 1995; Netzer 2015) of active galactic nuclei (AGNs). However, the structure of the dusty torus remains largely undetermined partly because it cannot be readily resolved, despite of a few successful attempts (e.g., Imanishi et al. 2018; García-Burillo et al. 2019; Gravity Collaboration et al. 2020). Some phenomenological torus models in which the morphology and distribution of dusty clouds are predefined are proposed. Then the efforts are focused on solving the sophisticated radiative transfer and obtaining the corresponding spectral energy distributions (SEDs) at near- to mid-infrared bands. These models can be roughly divided into three categories, i.e., a smooth torus (e.g., Fritz et al. 2006), a clumpy torus (e.g., Nenkova et al. 2008a,b), or a mixture of these two (e.g., Siebenmorgen et al. 2015).

Observationally speaking, the dusty torus manifests itself by various multi wavelength spectroscopic signatures. For instance, gas in the dusty torus can induce heavy X-ray obscuration (with X-ray column density $N_{\rm H}^{\rm X}$ to be more than 10^{24} cm^{-2}) if our line of sight is nearly edge-on. The dusty torus can absorb a significant fraction of AGN UV-to-optical continuum emission and re-emit mainly at mid-infrared (MIR) bands, thereby making the AGN intrinsic UV-to-optical SEDs much redder. In addition to the strong MIR continuum emission, the inner torus region can emit prominent silicate emission lines at 9.7 μm and 18 μm due to Si-O stretching and bending modes. Such features have indeed been detected by the *Spizter*/IRS spectroscopic observations (e.g., Siebenmorgen et al. 2005; Hao et al. 2005; Shi et al. 2006).

According to the simplest AGN unification model, if our line of sight is roughly face-on, we can directly detect emission from the central engine, the broad emission-line region, and the inner torus region. Therefore, we expect such AGNs to show unambiguous broad emission lines in their UV/optical spectra (classified as optical type 1), unobscured X-ray power-law emission and the 9.7 μm and

18 μm silicate emission features. In contrast, if the viewing angle is nearly edge-on, our line of sight is obscured by the dusty torus. Hence, such AGNs show X-ray spectra with heavy obscuration and lack broad emission lines (classified as optical type 2). Their silicate features are also expected to be observed as absorption (e.g., Siebenmorgen et al. 2004; Shi et al. 2006).

In reality, the relations among these dusty torus signatures are much more complex than expected. For example, optical type 2 AGNs with silicate emission features have been observed (Sturm et al. 2006; Nikutta et al. 2009). Shi et al. (2006) systematically investigated the X-ray absorption and the silicate feature of 97 AGNs with various types. They found that there is a connection between $N_{\rm H}^{\rm X}$ (inferred mostly from hardness ratios, which might be biased; see, e.g., Li et al. 2019) and the silicate feature (see Eq. (2) for the definition) which is consistent with the expectations of the simplest AGN unification model. However, the scatters of the connection are quite large. Therefore, they proposed that the torus structure should be complex and clumpy. In addition, Goulding et al. (2012) studied 20 nearby Compton-thick AGNs and pointed out that, at least for Compton-thick AGNs, the observed silicate absorption feature might be caused by galaxy-scale dust rather than a compact dusty torus near the central engine.

The study of dusty torus multi wavelength signatures can benefit from more complete AGN multi wavelength surveys. One of these surveys is the *Swift*/BAT all-sky survey (Baumgartner et al. 2013). The resulting AGN sample is complete with respect to X-ray absorption since the *Swift*/BAT ultra-hard (14–195 keV) band X-ray can penetrate through obscuring gas clouds with $N_{\rm H}^{\rm X} > 10^{24}$ cm^{-2}. Thanks to the wide X-ray spectroscopic coverage (0.3–195 keV), the X-ray properties (especially $N_{\rm H}^{\rm X}$) of each AGN were robustly measured (Ricci et al. 2015, 2017a). Meanwhile, the spectroscopic follow-up surveys were performed for a large fraction of this sample (hereafter BASS;[1] Koss et al. 2017). Furthermore, a significant fraction of the BASS AGNs also have *Spitzer*/IRS spectroscopic coverage which enables us to examine their silicate features. Therefore, this sample is ideal for us to explore the nature and structure of the dusty torus.

This paper is laid out as follows. In Section 2, we describe our sample construction and data analyses. In Section 3, we present our results. In Section 4, we discuss the implications of our results. Our conclusions are summarized in Section 5.

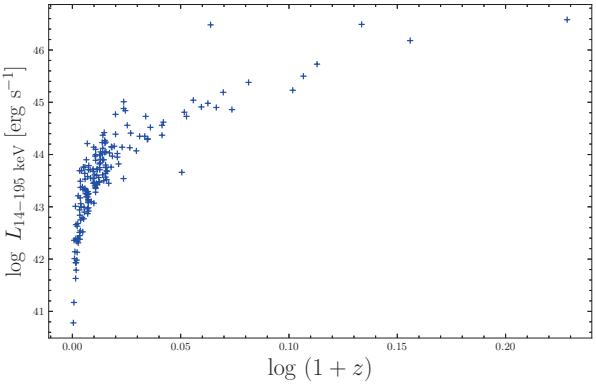

Fig. 1 The distribution of our sample in the 14–195 keV X-ray luminosity vs. redshift diagram.

2 SAMPLE CONSTRUCTION AND DATA REDUCTION

Our parent sample consists of 836 AGNs from the first 70-month observations of the unprecedented deep ultra-hard X-ray (14–195 keV) survey of the Burst Alert Telescope on the *Swift* Space satellite. Thanks to the wide X-ray spectroscopic coverage (0.3–195 keV), the X-ray properties (e.g., $N_{\rm H}^{\rm X}$ and the intrinsic X-ray luminosity, $L_{14-195\ \rm keV}$) of all 836 AGNs were well determined and the resulting catalog is publicly available (Ricci et al. 2015, 2017a). Therefore, compared with Shi et al. (2006), our AGNs have more reliable $N_{\rm H}^{\rm X}$ measurements.

For these 836 AGNs, we use their published counterparts (see Baumgartner et al. 2013) to cross-match (by name) with the Combined Atlas of Sources with Spitzer IRS Spectra (CASSIS[2]) database (Lebouteiller et al. 2011) to construct a new sample, which consists of 208 AGNs. Five sources are rejected since their *Spitzer*/IRS spectra do not have spectroscopic coverage around the 9.7 μm silicate feature. The remaining 203 AGNs are then cross-matched (by name) with the BASS catalog (Koss et al. 2017) to obtain their optical spectroscopic measurements. Most of the AGNs (185/203) in our sample have optical spectroscopic coverage. However, for 10 out of the 185 AGNs, their optical measurements and types are absent. Therefore, we reject these 10 sources. Our final sample, which consists of 175 AGNs, enables us to study the dusty torus in three spectroscopic respects, i.e., X-ray absorption, optical type, and the silicate feature. Their luminosity and redshift ranges are presented in Figure 1.

We perform the 9.7 μm silicate feature measurements by using *DeblendIRS*[3] (Hernán-Caballero et al. 2015) to fit *Spitzer*/IRS spectra. *DeblendIRS* is an *IDL* package that fit-

[1] For more details, refer to https://www.bass-survey.com
[2] For more details, refer to https://cassis.sirtf.com/.
[3] For more details, refer to http://www.denebola.org/ahc/deblendIRS/.

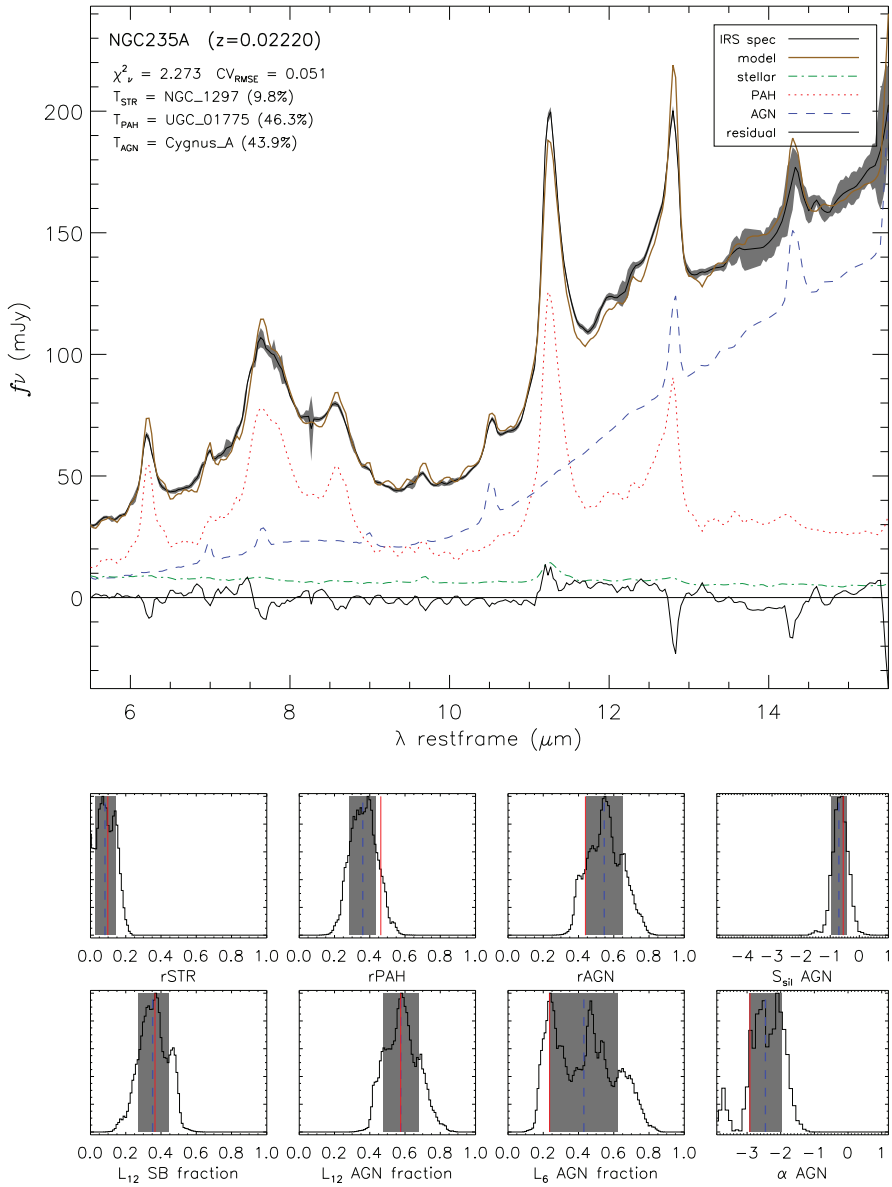

Fig. 2 A typical `deblendIRS` decomposed AGN IRS spectrum (*top*). The lower panels show the probability distributions of the fitting parameters (for their definitions, refer to Sect. 2), where the red solid and blue dashed lines represent the best-fitting results and the expectations of the distributions. The shaded regions indicate the 1σ uncertainties.

s the MIR spectra with a linear combination of three spectral templates, i.e., a "pure" AGN template, a "pure" stellar template, and a "pure" Polycyclic Aromatic Hydrocarbon (PAH, which accounts for the interstellar emission) template. The templates are constructed from real *Spitzer*/IRS spectra, which are dominated by a single physical component (i.e., AGN, stellar, or interstellar). For each AGN template, the silicate strength and the slope (α) of a power-law continuum between 8.1 μm and 12.5 μm are pre-measured. The silicate strength is defined as

$$S_{\rm Sil} = \ln \frac{F(\lambda_p)}{F_C(\lambda_p)}, \qquad (1)$$

where $F(\lambda_p)$ and $F_C(\lambda_p)$ stand for the maximum flux density of the silicate line profile near 9.7 μm and the corresponding flux density of the underlying continuum profile, respectively. Note that for sources with negative values of $S_{\rm Sil}$, we expect the optical depth of the silicate absorption $\tau_{9.7} = -S_{\rm Sil}$. Therefore, *DeblendIRS* can provide the best-fitting results and uncertainties for the contribution of AGN emission at rest-frame 6 μm , 12 μm , and 5–15 μm (hereafter L_6 AGN fraction, L_{12} AGN fraction and rAGN, respectively), the stellar contribution at rest-frame 12 μm and 5–15 μm (hereafter L_{12} SB fraction and rSTR, respectively), the interstellar contribution at rest-frame 5–15 μm (hereafter rPAH), $S_{\rm Sil}$ and α (for more technical details,

refer to sect. 2 of Hernán-Caballero et al. 2015). An example of our *DeblendIRS* fitting results is shown in the upper panel of Figure 2. It is evident that the best-fitting model explains the data well.

Unlike our work, Ichikawa et al. (2019) adopted another *IDL* routine *DecompIR* (Mullaney et al. 2011) to decompose the multi-band IR (from $\sim$ 3 μm to $\sim$ 200 μm) photometric data and neglected the *Spitzer*/IRS spectra. There are 160 sources in both our final sample and the catalog of Ichikawa et al. (2019). To further justify our fitting results, we compare our best-fitting 12 μm monochromic luminosities (hereafter $\lambda L_\lambda(12\,\mu\mathrm{m})$) with those of Ichikawa et al. (2019) (see Fig. 3). Our results are well consistent with those of Ichikawa et al. (2019); indeed, the median ratio between our and their $\lambda L_\lambda(12\,\mu\mathrm{m})$ is 1.06. Therefore, we argue that our AGN measurements are reliable.

3 RESULTS

3.1 Silicate Strength and X-ray Absorption

Following Shi et al. (2006), we first explore the relationship between the silicate feature and $N_{\rm H}^{\rm X}$. Shi et al. (2006) defined the following quantity,

$$R_{9.7} = \frac{F(\lambda_p) - F_C(\lambda_p)}{F_C(\lambda_p)} \qquad (2)$$

where negative/positive $R_{9.7}$ suggests silicate absorption/emission. It is straightforward to show that $R_{9.7} = \exp(S_{\rm Sil}) - 1$ and approaches $S_{\rm Sil}$ if $S_{\rm Sil}$ is close to zero. Figure 4 plots $R_{9.7}$ as a function of $N_{\rm H}^{\rm X}$ for our final sample. We confirm that, consistent with the result of Shi et al. (2006), there is a weak anti-correlation between $R_{9.7}$ and $N_{\rm H}^{\rm X}$ (the Spearman's $\rho = -0.63$ and the corresponding p-value is 4.5×10^{-21}). That is, heavily X-ray obscured AGNs tend to show silicate absorption and absence of broad emission lines, and vice versa. We fit the data with the linear relation $R_{9.7} = A + B \log N_{\rm H}^{\rm X}$ via the MCMC algorithm.[4] The fitting results are $A = 4.1^{+0.6}_{-0.5}$ and $B = -0.20^{+0.03}_{-0.03}$, which is in agreement with the best-fitting results of Shi et al. (2006). However, the scatters of the anti-correlation are quite large. The large scatters might be caused by several different factors. For example, the gas-to-dust ratio may vary among different AGNs. As pointed out by Shi et al. (2006), the scatter of this ratio should be more than two orders of magnitude, which is unlikely to be the case here. Another possibility is that the heavy X-ray absorption is caused by the gas lying closer to the central engine than the dusty torus, e.g., the broad emission-line gas. However, this scenario cannot explain the fact that many of these AGNs, which show heavy X-ray obscuration but different silicate strengths, are actually optical type 1.9 or type 2 sources, i.e., sources with strong dust extinction. Other possibilities are that the dusty torus is not a smooth "donut" but a highly clumpy one, the line-of-sight absorption is time-dependent (e.g., Yang et al. 2016; Jaffarian & Gaskell 2020), and/or the radiative transfer may also play a role.

[4] We use *lnr.py* to perform the fit. This *Python* code is available at https://www.astro.princeton.edu/~sifon/pycorner/lnr/.

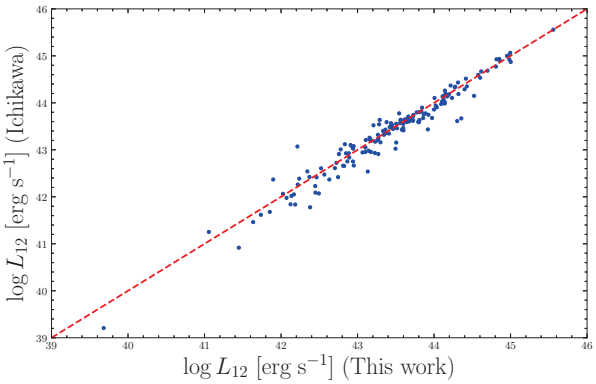

Fig. 3 Comparison between our measurements of $\lambda L_\lambda(12\,\mu\mathrm{m})$ with those of Ichikawa et al. (2019). The red dashed line indicates the one-to-one relation. Our results are in good agreement with those of Ichikawa et al. (2019).

3.2 Silicate Strength and Broad-Hα-line-inferred Extinction

For a subsample of AGNs with broad Hα emission lines, Shimizu et al. (2018) adopted the empirical relation between X-ray and broad Hα luminosities and the absorption-corrected X-ray luminosities to obtain the intrinsic broad Hα luminosities. By comparing the in-

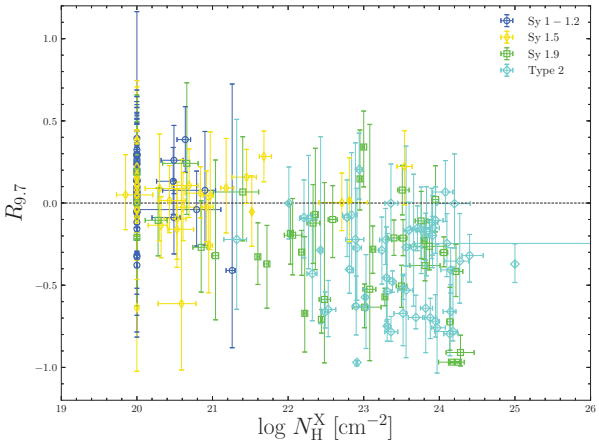

Fig. 4 $R_{9.7}$ as a function of $N_{\rm H}^{\rm X}$ for our selected sources. The blue open circles, yellow open diamonds, green open squares, and cyan open diamonds represent type 1–1.2, type 1.5, type 1.9, and type 2 AGNs, respectively.

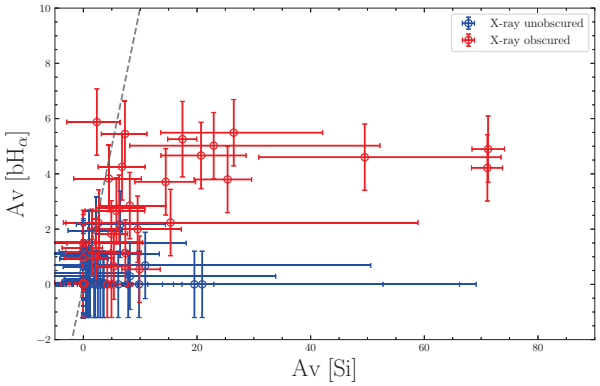

Fig. 5 The optical extinction of the broad Hα line (A_V[bHα]) versus the silicate strength-inferred V-band extinction (A_V[Si]). The blue and red symbols indicate X-ray unobscured (i.e., $N_{\rm H}^{\rm X} < 10^{21.5}$ cm^{-2}) and obscured sources (i.e., $N_{\rm H}^{\rm X} \geq 10^{21.5}$ cm^{-2}), respectively. Note that the uncertainties of A_V[bHα] are caused by both the measurement errors of the broad Hα fluxes and a systematic uncertainty of 1.2 mag (Shimizu et al. 2018). The dashed line indicates the one-to-one relation.

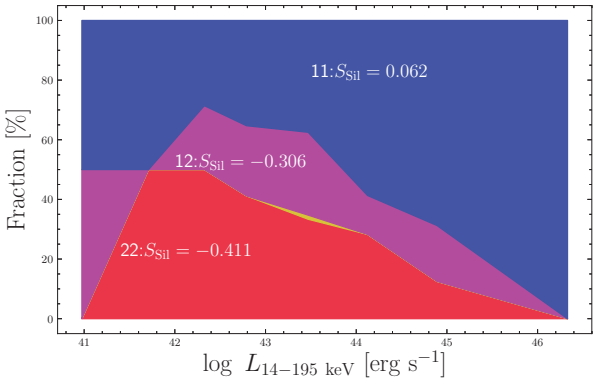

Fig. 6 Relative fractions of AGN types as a function of the AGN 14-195 keV X-ray luminosity. The blue shaded region represents type-11 sources (optical type 1 and X-ray unobscured). The purple shaded region represents type-12 sources (optical type 1 and X-ray obscured). The yellow shaded region represents type-21 sources (optical type 2 and X-ray unobscured). The red shaded region represents type-22 sources (optical type 2 and X-ray obscured). The median silicate strength values for type-11, type-12 and type-22 are annotated, where positive values indicate silicate emission and vice versa. There is only one type-21 AGN and its silicate strength is not shown.

trinsic broad Hα luminosities with the observed ones, Shimizu et al. (2018) estimated the optical extinction of the broad-line region (hereafter A_V[bHα]). Then, they explored the relation between A_V[bHα] and $N_{\rm H}^{\rm X}$ and found that a significant fraction of AGNs have orders of magnitude higher $N_{\rm H}^{\rm X}$ than the A_V[bHα]-inferred values by assuming a Galactic ratio of $N_{\rm H}$ to A_V (Draine 2011). The population of optical type 1 AGNs with heavy X-ray absorption has also been explored by Merloni et al. (2014) who used the 1310 XMM-COSMOS AGNs as well as several previous works (e.g., Burtscher et al. 2016; Schnorr-Müller et al. 2016).

We first investigate the relation between A_V[bHα] and the silicate strength-inferred V-band extinction (hereafter A_V[Si]) where A_V[Si] is estimated from $S_{\rm Sil}$ following the methodology presented in section 3 of Shi et al. (2006). Note that, for sources with silicate emission lines, we set A_V[Si] $= 0$. For the 93 AGNs in our final sample that have broad Hα measurements, we follow Merloni et al. (2014) and classify them into two categories according to $N_{\rm H}^{\rm X}$, i.e., the X-ray unobscured (i.e., $N_{\rm H}^{\rm X} < 10^{21.5}$ cm^{-2}) and obscured sources (i.e., $N_{\rm H}^{\rm X} \geq 10^{21.5}$ cm^{-2}). The results are shown in Figure 5. For X-ray unobscured AGNs, their A_V[bHα] and A_V[Si] values are both small. However, for X-ray obscured AGNs, A_V[bHα] and A_V[Si] are large and the former is on average much smaller than the latter (see Sect. 4.2 for the discussions of the possible physical reasons).

Following Merloni et al. (2014), we further classify our final sample into four categories, i.e., type-11 (optical type 1 and $N_{\rm H}^{\rm X} < 10^{21.5}$ cm^{-2}), type-12 (optical type 1 and $N_{\rm H}^{\rm X} \geq 10^{21.5}$ cm^{-2}), type-21 (optical type 2 and $N_{\rm H}^{\rm X} < 10^{21.5}$ cm^{-2}), and type-22 (optical type 2 and $N_{\rm H}^{\rm X} \geq 10^{21.5}$ cm^{-2}). Their relative fraction as a function of X-ray luminosities are presented in Figure 6. Unlike Merloni et al. (2014), we also can calculate the median value of $S_{\rm Sil}$ (i.e., $-\tau_{9.7}$) for each type. Consistent with our expectations, type-11/type-22 sources on average have silicate emission/absorption features. However, type-12 AGNs tend to show prominent silicate absorption, which is consistent with the result of Figure 4. Among them, the silicate absorption in optical type 1.5 is weak or nearly absent; the silicate absorption in optical type 1.9 is rather strong. Our results indicate that, at least for the optical type 1.9 AGNs in the type-12 population, the excess of X-ray absorption might not be caused by dust-free broad-line gas.

In conclusion, the results of Figures 4–6 along with previous works (e.g., Shi et al. 2006; Merloni et al. 2014) suggest that the distributions and structures of obscuring gas and extinction dust are very complex.

4 DISCUSSION

As demonstrated in Section 3, $S_{\rm Sil}$, $N_{\rm H}^{\rm X}$, and A_V[bHα] often show discrepant results, which might be caused by various factors as discussed below.

4.1 Smooth Torus vs. Clumpy Torus

One possible explanation is that the dusty torus is not a smooth "donut" but a highly clumpy one. To test this sce-

nario, we compare our results in Figures 4–6 with a smooth torus model of Fritz et al. (2006) and a clumpy torus model of Nenkova et al. (2008a,b), respectively.

4.1.1 *Testing the smooth torus model*

One popular smooth torus model is introduced by Fritz et al. (2006). In this model, the dust mass density is a function of both radius (with respect to the central black hole) and inclination angle (i), i.e.,

$$\rho(r, i) = \rho_0 r^{-q} \mathrm{e}^{-\gamma|\cos(i)|}, \quad (3)$$

where ρ_0 is determined by the equatorial-plane-dust optical depth at 9.7 μm ($\tau^0_{9.7}$), q is the radial power-law index, and γ is the polar exponential index, respectively. The torus inner radius is determined by the dust sublimation radius; the ratio of the outer radius to the inner radius (Y) is allowed to vary as a free parameter. Another parameter is the angular region occupied by the dust (Θ). The smooth torus is then illuminated by a central isotropic point AGN emission with a fixed SED of Schartmann et al. (2005). The radiation emitted by the smooth torus is calculated by solving the radiative transfer equations (for more details, see Section 2 of Fritz et al. 2006).

The explored parameter ranges, which are introduced by Feltre et al. (2012), are listed in Table 1; the covered physical space is wider than the original work of Fritz et al. (2006). For each of the 24 000 smooth-torus SED templates, we first estimate its $S_{\rm Sil}$ by following the methodology in section 5.2 of Hernán-Caballero et al. (2015). Second, we calculate the corresponding line-of-sight $N_{\rm H}$ and the V-band extinction as follows. The line-of-sight optical depth at 9.7 μm is

$$\tau_{9.7} = \tau^0_{9.7} \times \mathrm{e}^{-\gamma|\cos(\theta)|}, \quad (4)$$

and the corresponding extinction is

$$\begin{aligned} \frac{A_{9.7}}{\rm mag} &\equiv 2.5 \log_{10}\left[F_C(\lambda_p)/F(\lambda_p)\right] \\ &= 2.5 \log_{10}\left[e^{\tau_{9.7}}\right] = 1.086\tau_{9.7} \end{aligned}. \quad (5)$$

The V-band extinction is assumed to be $A_V = 19 \times A_{9.7}$ (Roche & Aitken 1985). Then, the corresponding line-of-sight $N_{\rm H}$ is estimated by considering the dust-to-gas ratio of $A_V/N_{\rm H} = 0.62 \times 10^{-21}$ mag cm^2 (Savage & Mathis 1979).

The relation between $N_{\rm H}$ and $S_{\rm Sil}$ for the smooth torus model is presented in Figure 7. It is evident that SEDs with silicate absorption (i.e., negative $S_{\rm Sil}$) always correspond to significant line-of-sight $N_{\rm H}$ (i.e., $> 10^{22.5}$cm^{-2}). Therefore, the smooth torus model cannot explain AGNs with small $N^X_{\rm H}$ but evident silicate absorption. The relation between A_V and $S_{\rm Sil}$ is presented in Figure 8. Again, the smooth torus model cannot explain our observations.

Table 1 The Parameter Space of the Smooth Torus Model of Fritz et al. (2006)

Θ (degree)	60°, 100°, 140°
q	0.00, 0.25, 0.50, 0.75, 1.0
i (degree)	0°, 10°, 20° , 30°, 40°, 50°, 60°, 70°, 80°, 90°
γ	0.0, 2.0, 4.0, 6.0
$\tau^0_{9.7}$	0.1, 0.3, 0.6, 1.0, 2.0, 3.0, 6.0, 10.0
Y	10, 30, 60, 100, 150

Θ, q, i, γ, $\tau^0_{9.7}$, and Y represent the angular region occupied by the dust, the radial power-law index, the inclination angle, the polar exponential index, the equatorial-plane-dust optical depth at 9.7 μm , and the ratio of the outer radius to the inner radius, respectively.

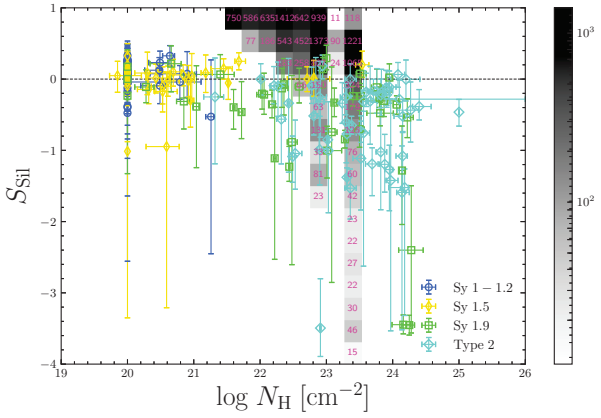

Fig. 7 $S_{\rm Sil}$ as a function of $N_{\rm H}$. The blue-open circles, yellow-open-thin diamonds, green-open squares, and cyan-open diamonds represent the observations (i.e., $S_{\rm Sil}$ and $N^X_{\rm H}$) of optical Type 1-1.2, Type 1.5, Type 1.9, and Type 2 AGNs, respectively. The grey histogram represents the two-dimensional distribution of $S_{\rm Sil}$ and $N_{\rm H}$ for the smooth torus model of Fritz et al. (2006). The number of SEDs in each bin is labeled. The smooth torus model cannot account for AGNs with small $N^X_{\rm H}$ but evident silicate absorption.

4.1.2 *Testing the clumpy torus model*

A clumpy torus model is presented by Nenkova et al. (2008a,b). According to this model, in the radial direction, dusty clouds with the same V-band extinction (τ_V) are distributed as r^{-q}; in the azimuthal direction, the dusty clouds follow a Gaussian distribution, i.e., $e^{-((90-i)/\sigma)^2}$, where σ is the Gaussian width. Other parameters are the ratio of the outer radius to the inner one (Y) and the cloud number along the equatorial plane (N_0). The clumpy torus is then illuminated by a central AGN source with an SED shape of Rowan-Robinson (1995).

The explored parameter space of the clumpy torus model is listed in Table 2. Then, for each of the 1 247 400 resulting SEDs, we estimate the corresponding $S_{\rm Sil}$. The line-of-sight $N_{\rm H}$ and V-band extinction are calculated as follows. First, the line-of-sight cloud number is

$$n_{\rm los} = N_0 \times \mathrm{e}^{-(\frac{90-i}{\sigma})^2}. \quad (6)$$

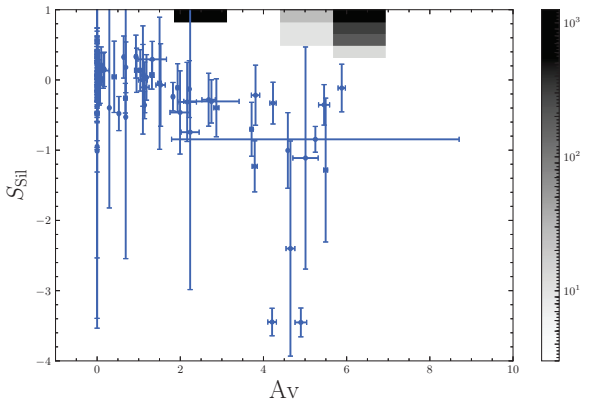

Fig. 8 $S_{\rm Sil}$ as a function of A_V. The blue dots represent the observations (i.e., $S_{\rm Sil}$ and A_V[bH$_\alpha$]) of our final sample. The grey histogram represents the two-dimensional distribution of $S_{\rm Sil}$ and A_V for the smooth torus model of Fritz et al. (2006). The number of SEDs in each bin is indicated by the color bar. The smooth torus model cannot account for AGNs with small V-band extinction but evident silicate absorption.

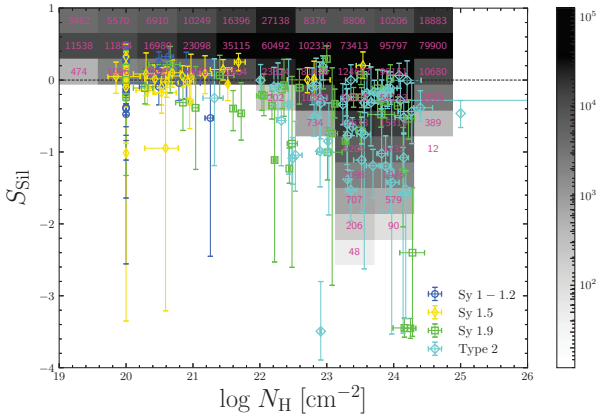

Fig. 9 Same as Fig. 7 but for the clumpy torus model of Nenkova et al. (2008a).

Considering again the dust-to-gas ratio of Savage & Mathis (1979), the observed hydrogen column density $N_{\rm H}$ is

$$N_{\rm H} = \frac{n_{\rm los} \times 1.086\tau_V}{0.62 \times 10^{-21}}\ {\rm cm}^{-2}. \quad (7)$$

The relation between $N_{\rm H}$ and $S_{\rm Sil}$ (A_V and $S_{\rm Sil}$) for the clumpy torus model is presented in Figure 9 (Fig. 10). Compared with the smooth torus model, the clumpy torus model can explain the observations for most of our sources, especially AGNs with evident silicate absorption and small line-of-sight $N_{\rm H}$ or V-band extinction.

4.2 Additional Gas and Dust Obscuration

The discrepancy between $S_{\rm Sil}$ and $N_{\rm H}^{\rm X}$ or A_V[bHα] might also be caused by other effects. For instance, as pointed out

Table 2 The Parameter Space of the Nenkova et al. (2008a) Clumpy Torus Template Library

σ (degree)	15°, 20°, 25°, 30°,35°,40°,45°,50°,55°, 60°,65°,70°
q	0.0, 0.5, 1.0, 1.5, 2.0, 2.5, 3.0
i (degree)	0°, 10°, 20° , 30°, 40°, 50°, 60°, 70°, 80°, 90°
$\tau_{\rm V}$	10, 20, 40, 60, 80, 120, 160, 200, 300
N_0	1, 2, 3, 4, 5, 6, 7, 8, 9, 10, 11, 12, 13, 14, 15
Y	5, 10, 20, 30, 40, 50, 60, 70, 80, 90, 100

σ, q, i, $\tau_{\rm V}$, N_0 and Y represent the polar distribution Gaussian-function width, the radial power-law index, the inclination angle, the V-band optical depth for each dust cloud, the cloud number along the equatorial plane, and the ratio of outer to inner radius, respectively.

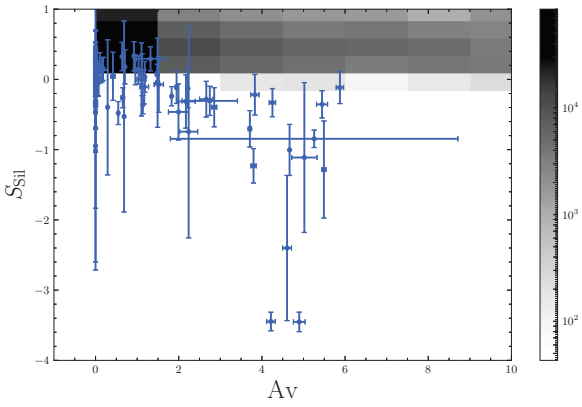

Fig. 10 Same as Fig. 8 but for the clumpy torus model of Nenkova et al. (2008a).

by Goulding et al. (2012), the silicate absorption might be contributed by dust located in the host galaxy rather than the AGN torus. If so, we would expect that sources with larger inclination angles should have stronger silicate absorption. Following Goulding et al. (2012), we use the ratio of the major isophotal diameter to the minor one (hereafter $R25$) as introduced in the Third Reference Catalog of Bright Galaxies (Corwin et al. 1994) to probe the galaxy inclination angle (sources with smaller $R25$ values might tend to be more face-on). For the 153 sources in the final sample, we can obtain their $R25$. We then divide these sources into two groups according to their positions relative to the best-fitting relation between $R_{9.7}$ and $N_{\rm H}^{\rm X}$ (see Sect. 3.1). That is, we calculate the difference ($\Delta R_{9.7}$) between the observed $R_{9.7}$ and the predicted one from the best-fitting relation. Group 1 (2) sources have positive (negative) $\Delta R_{9.7}$. The distributions of $\log R25$ for the two groups are presented in Figure 11. We also perform the Anderson-Darling test to check the differences between the two distributions. We find that the null hypothesis that the two distributions are drawn from the same population cannot be rejected (i.e., the p-value of the null hypothesis is much larger than 0.05). Therefore, we conclude that the discrepancy between $S_{\rm Sil}$ and $N_{\rm H}^{\rm X}$ are unlikely to be caused by galaxy-scale dust absorption.

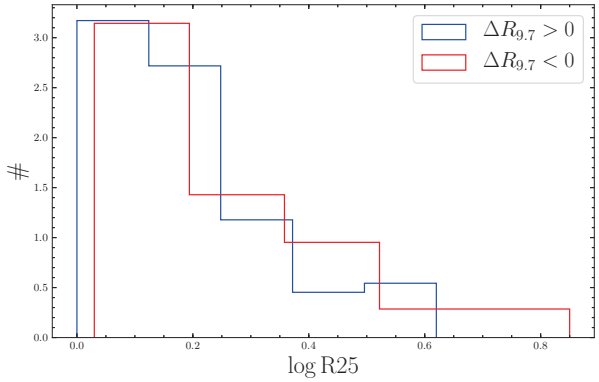

Fig. 11 Distributions of $\log R25$ for two groups of sources with different $\Delta R_{9.7}$. The distributions are normalized to ensure that the total area within each histogram is equal to one. The distribution of $\log R25$ for sources with positive $\Delta R_{9.7}$ (i.e., less silicate absorption) is similar to the distribution of $\log R25$ for sources with negative $\Delta R_{9.7}$.

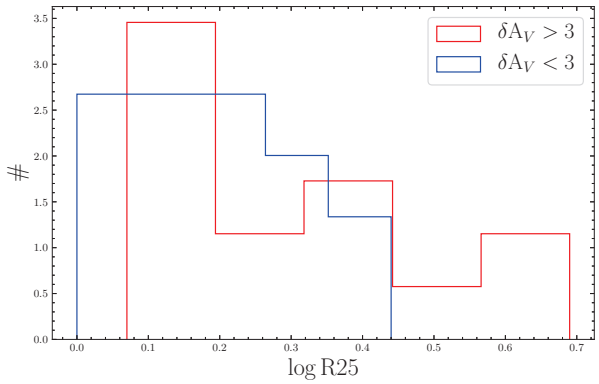

Fig. 12 Same as Fig. 11, but for two groups of sources with different δA_V. The two distributions are statistically consistent.

We then check the discrepancy between $S_{\rm Sil}$ and $A_V[{\rm bH}\alpha]$ as a function of $R25$. We define $\delta A_V = (A_V[{\rm Si}] - A_V[{\rm bH}\alpha])/A_V[{\rm bH}\alpha]$ and divide the sources with non-zero $A_V[{\rm Si}]$ and $A_V[{\rm bH}\alpha]$ into two groups, i.e., group 1 with $\delta A_V > 3$ and group 2 with $\delta A_V < 3$. Again, we find that the two groups share the same distribution of $\log R25$. Therefore, the discrepancy between $S_{\rm Sil}$ and $A_V[{\rm bH}\alpha]$ is also unlikely to be mainly driven by galaxy-scale dust absorption.

The discrepancy between $S_{\rm Sil}$ and $A_V[{\rm bH}\alpha]$ for X-ray obscured sources might be explained as follows. First, as mentioned in Section 3.2, the estimates of $A_V[{\rm bH}\alpha]$ rely on the empirical relation between X-ray and broad Hα luminosities, which is obtained for type 1.0 or 1.2 Seyferts. However, type 1.0 or 1.2 Seyferts might also suffer dust extinction to some degree; therefore, $A_V[{\rm bH}\alpha]$ is almost always an under-estimation of true dust extinction. Second, for X-ray obscured sources, their hidden broad emission-line fluxes might be scattered into our line of sight (indeed, spectropolarimetry observations revealed high-polarization broad emission lines in at least some of our X-ray obscured sources, e.g., Mrk 3, Mrk 348, and Mrk 1210; see, e.g., Miller & Goodrich 1990; Tran et al. 1992). That is, the observed broad Hα flux is larger than the direct broad Hα flux (which is heavily absorbed by the dusty torus), i.e.,

$F_{\rm obs}({\rm bH}\alpha)$=$F_{\rm int}({\rm bH}\alpha)\exp(-\tau({\rm H}\alpha))$+ $F_{\rm sct}({\rm bH}\alpha)$,

where $F_{\rm int}({\rm bH}\alpha)$, $\tau({\rm H}\alpha)$, and $F_{\rm sct}({\rm bH}\alpha)$ are the intrinsic broad Hα flux, the optical depth of Hα, and the scattered broad Hα flux, respectively. Note that the scatted light is assumed to be not absorbed by the dusty torus. If τ is larger than 9 (i.e., $A_V \geq 11.95$ for the extinction law of Cardelli et al. 1989), the direct broad-line flux is extinguished and $F_{\rm obs}({\rm bH}\alpha) \cong f_{\rm sc}F_{\rm int}({\rm bH}\alpha)$, where $f_{\rm sc}$ is the ratio of $F_{\rm sct}({\rm bH}\alpha)$ to $F_{\rm int}({\rm bH}\alpha)$. If so, for such sources, the inferred $A_V[{\rm bH}\alpha]$ is about $4.02 + 3.32\log(0.05/f_{\rm sc})$, i.e., $A_V[{\rm bH}\alpha]$ might thus be systematically underestimated compared to the actual one given that $f_{\rm sc}$ is about a few percent (e.g., Reynolds et al. 1997). Third, it is also possible that the broad Hα in some type 1.9 AGNs might be produced by strong outflows (i.e., they are actually type 2 AGNs). One such example is 2MASX J07595347+2323241, whose broad Hα is surprisingly narrow. In fact, its Hα-inferred virial black hole mass is two orders of magnitude smaller than the expectation of the $M_{\rm BH} - \sigma$ relation or the infrared broad Paβ-inferred one (Ricci et al. 2017b). Therefore, possibly due to the combined effect of the aforementioned factors, $A_V[{\rm bH}\alpha]$ is expected to be systematically smaller than the silicate strength-inferred A_V, at least for some of our X-ray obscured AGNs.

Dust-free gas (e.g., gas in the broad-line regions) can provide additional X-ray obscuration. However, they cannot contribute to silicate absorption or Hα extinction. As mentioned in Section 3 (also see Figs. 4 and 6), dust-free gas cannot fully account for the discrepancy between $S_{\rm Sil}$ and $N_{\rm H}^{\rm X}$ since many sources are type 2 sources.

5 SUMMARY OF CONCLUSIONS

We decompose the *Spitzer*/IRS spectra of 175 BASS AGNs to measure their silicate strengths and compare them with absorption signatures in X-rays and broad Hα emission. Our results are summarized as follows.

1. Consistent with previous work (Shi et al. 2006), we confirm a weak relation between the silicate strength and $N_{\rm H}^{X}$ using more accurate $N_{\rm H}^{\rm X}$ measurements; however, the scatter of the relation is quite large (see Fig. 4 and Sect. 3.1).
2. For X-ray unobscured AGNs, the silicate strength and the Hα-inferred V-band extinction are both small; while for X-ray obscured ones, the silicate strength is

much stronger than the expectation of the Hα-inferred V-band extinction (see Fig. 5 and Sect. 3.2). This result and the previous one suggest that the distributions and structures of obscuration gas and extinction dust are very complex.

3. We test our data against two popular torus models, i.e., the smooth torus model (see Sect. 4.1.1) of Fritz et al. (2006) and the clumpy torus model (see Sect. 4.1.2) of Nenkova et al. (2008a). We find that the clumpy torus model is more consistent with our observations than the smooth one.

Acknowledgements We thank the referee for his/her helpful comments that improved the manuscript. J.X., M.Y.S., Y.Q.X., and J.Y.L. acknowledge the support from the National Natural Science Foundation of China (Nos. 11973002, 11890693 and 11421303), the China Postdoctoral Science Foundation (2016M600485), and the CAS Frontier Science Key Research Program (QYZDJ-SSW-SLH006), and the K.C. Wong Education Foundation.

The Combined Atlas of Sources with Spitzer IRS Spectra (CASSIS) is a product of the IRS instrument team, supported by NASA and JPL. CASSIS is supported by the "Programme National de Physique Stellaire" (PNPS) of CNRS/INSU co-funded by CEA and CNES and through the "Programme National Physique et Chimie du Milieu Interstellaire" (PCMI) of CNRS/INSU with INC/INP co-funded by CEA and CNES.

References

Antonucci, R. 1993, ARA&A, 31, 473
Baumgartner, W. H., Tueller, J., Markwardt, C. B., et al. 2013, ApJS, 207, 19
Burtscher, L., Davies, R. I., Graciá-Carpio, J., et al. 2016, A&A, 586, A28
Cardelli, J. A., Clayton, G. C., & Mathis, J. S. 1989, ApJ, 345, 245
Corwin, Harold G., J., Buta, R. J., & de Vaucouleurs, G. 1994, AJ, 108, 2128
Draine, B. T. 2011, Physics of the Interstellar and Intergalactic Medium (Princeton: Princeton University Press)
Feltre, A., Hatziminaoglou, E., Fritz, J., & Franceschini, A. 2012, MNRAS, 426, 120
Fritz, J., Franceschini, A., & Hatziminaoglou, E. 2006, MNRAS, 366, 767
García-Burillo, S., Combes, F., Ramos Almeida, C., et al. 2019, A&A, 632, A61
Goulding, A. D., Alexander, D. M., Bauer, F. E., et al. 2012, ApJ, 755, 5
Gravity Collaboration, Pfuhl, O., Davies, R., et al. 2020, A&A, 634, A1
Hao, L., Spoon, H. W. W., Sloan, G. C., et al. 2005, ApJL, 625, L75
Hernán-Caballero, A., Alonso-Herrero, A., Hatziminaoglou, E., et al. 2015, ApJ, 803, 109
Ichikawa, K., Ricci, C., Ueda, Y., et al. 2019, ApJ, 870, 31
Imanishi, M., Nakanishi, K., Izumi, T., & Wada, K. 2018, ApJL, 853, L25
Jaffarian, G. W., & Gaskell, C. M. 2020, MNRAS, 493, 930
Koss, M., Trakhtenbrot, B., Ricci, C., et al. 2017, ApJ, 850, 74
Lebouteiller, V., Barry, D. J., Spoon, H. W. W., et al. 2011, ApJS, 196, 8
Li, J., Xue, Y., Sun, M., et al. 2019, ApJ, 877, 5
Merloni, A., Bongiorno, A., Brusa, M., et al. 2014, MNRAS, 437, 3550
Miller, J. S., & Goodrich, R. W. 1990, ApJ, 355, 456
Mullaney, J. R., Alexander, D. M., Goulding, A. D., & Hickox, R. C. 2011, MNRAS, 414, 1082
Nenkova, M., Sirocky, M. M., Ivezić, Ž., & Elitzur, M. 2008a, ApJ, 685, 147
Nenkova, M., Sirocky, M. M., Nikutta, R., Ivezić, Ž., & Elitzur, M. 2008b, ApJ, 685, 160
Netzer, H. 2015, ARA&A, 53, 365
Nikutta, R., Elitzur, M., & Lacy, M. 2009, ApJ, 707, 1550
Reynolds, C. S., Ward, M. J., Fabian, A. C., & Celotti, A. 1997, MNRAS, 291, 403
Ricci, C., Ueda, Y., Koss, M. J., et al. 2015, ApJL, 815, L13
Ricci, C., Trakhtenbrot, B., Koss, M. J., et al. 2017a, ApJS, 233, 17
Ricci, F., La Franca, F., Marconi, A., et al. 2017b, MNRAS, 471, L41
Roche, P. F., & Aitken, D. K. 1985, MNRAS, 215, 425
Rowan-Robinson, M. 1995, MNRAS, 272, 737
Savage, B. D., & Mathis, J. S. 1979, ARA&A, 17, 73
Schartmann, M., Meisenheimer, K., Camenzind, M., Wolf, S., & Henning, T. 2005, A&A, 437, 861
Schnorr-Müller, A., Davies, R. I., Korista, K. T., et al. 2016, MNRAS, 462, 3570
Shi, Y., Rieke, G. H., Hines, D. C., et al. 2006, ApJ, 653, 127
Shimizu, T. T., Davies, R. I., Koss, M., et al. 2018, ApJ, 856, 154
Siebenmorgen, R., Haas, M., Krügel, E., & Schulz, B. 2005, A&A, 436, L5
Siebenmorgen, R., Heymann, F., & Efstathiou, A. 2015, A&A, 583, A120
Siebenmorgen, R., Krügel, E., & Spoon, H. W. W. 2004, A&A, 414, 123
Sturm, E., Hasinger, G., Lehmann, I., et al. 2006, ApJ, 642, 81
Tran, H. D., Miller, J. S., & Kay, L. E. 1992, ApJ, 397, 452
Urry, C. M., & Padovani, P. 1995, PASP, 107, 803
Yang, G., Brandt, W. N., Luo, B., et al. 2016, ApJ, 831, 145